https://doi.org/10.5194/amt-2020-382
Preprint. Discussion started: 26 October 2020

Atmospheric Measurement Techniques Discussions

Eddies in motion: visualizing boundary-layer turbulence above an open boreal peatland using UAS thermal videos

Pavel Alekseychik[1,2], Gabriel Katul[3], Ilkka Korpela[4], Samuli Launiainen[1]

[1] Bioeconomy and Environment, Natural Resources Institute Finland, 00791 Helsinki, Finland

[2] Institute for Atmospheric and Earth System Research/Physics, Faculty of Science, P.O. Box 68, FI-00014 University of Helsinki, Finland

[3] Nicholas School of the Environment, and Department of Civil and Environmental Engineering, Duke University, Durham, NC, USA

[4] Department of Forest Sciences, University of Helsinki, P.O. Box 27, 00014 University of Helsinki

Correspondence to: Pavel Alekseychik (pavel.alekseychik@luke.fi)

Abstract. High resolution thermal infrared (TIR) imaging is opening up new vistas in biosphere-atmosphere heat exchange studies. The rapidly developing unmanned aerial systems (UAS) and specially designed TIR cameras offer opportunities for TIR survey with increasingly high resolution, reduced noise, prolonged flight times and better gimbals. A state-of-the-art science platform is assembled using a Matrice 210 V2 drone equipped with a Zenmuse XT2 thermal camera and deployed over a pristine boreal peatland with the aim to test its performance in a heterogeneous ecosystem with short vegetation. The study utilizes the capability of the UAS platform to hover for prolonged times (about 20 min) whilst recording high-frequency (1–30 Hz) TIR videos. A methodology to derive thermal signatures of near-ground coherent turbulent structures impinging on the land surface, surface temperature spectra and heat fluxes from the retrieved videos is developed. The size, residence time and movement of the coherent structures are computed from the surface temperature maps, and their dependency on atmospheric conditions is examined. A ground-based eddy-covariance system and a collocated meteorological setup are used for reference.

Keywords: atmospheric boundary layer, boreal peatland, coherent structures, drones, energy balance, infrared imaging, UAS, surface temperature, temperature power spectrum, turbulence.

1 Introduction

One of the long-standing problems in turbulence research, particularly turbulence in the planetary boundary layer (PBL), is the heat transfer between rough surfaces and the turbulent flow aloft. Eddies scour the surface and transport heat from the neighborhood of the roughness elements into the unobstructed flow. The precise nature of the eddies in terms of sizes and contact durations that effectively impinge and scour the surface to transport heat remains a formidable challenge and a subject of active research for several decades now (Owen and Thompson, 1963; Adrian, 2007). With rapid advancements in thermal infrared (TIR) imagery and image processing, a new arsenal of experimental methods can now enable progress on these issues and motivates the present work.

The present study focuses on the properties of large coherent turbulent structures, or dominant eddies as termed already by Taylor (1958). Taylor (1958) was the first to draw attention to the regular features in air temperature time series, which the subsequent analysis by Priestley (1959) linked to the thermals generated by surface roughness and buoyancy. Air parcels residing near the ground attain buoyancy upon receipt of heat from the ground and rise up, to become replaced by cooler air parcels descending from above, in a cyclical manner. Such ascending and descending air parcels reach the size of the entire

https://doi.org/10.5194/amt-2020-382
Preprint. Discussion started: 26 October 2020

Atmospheric Measurement Techniques Discussions

boundary layer, i.e. hundreds to thousands of meters across (Kaimal and Businger 1970, Kaimal et al. 1976). Estimating the size, shape, movement and time scales of such coherent structures remains a difficult task.

The principal applicability of TIR to turbulence studies has been established in several field studies to date. Some of the earliest experiments (Hoyano et al. 1999, Sugawara et al. 2001, Chudnovsky et al. 2004, Meier et al. 2010) used TIR made in an urban setting to determine the thermal properties of various surfaces, and to remotely estimate the components of the surface energy balance. Vogt et al. (2008) were the first to record thermal videos over a grass field, which was soon followed by Garai and Kleissl (2011) and a similar experiment to describe the temporal skin temperature variation on various urban surfaces (Christen and Vogt 2012). Those studies established the possibility to visualize and analyze different scales of turbulent eddies. Garai and Kleissl (2011) regretted that the largest of the coherent structures were apparently much bigger than the patch of ground and proposed that flying a camera suspended on a balloon at a few hundred meters above ground would improve detection of larger eddies. The current generation of multirotor UASs are now capable of carrying out this task.

None of the previous IR experiments has covered a surface area exceeding 100 m in diameter. The largest flat surface experiment so far is that of Garai and Kleissl (2013), where an area 275 x 207 m was imaged. A similar approach by Christen et al. (2012) used a camera with a very oblique imaging angle targeted at a complex urban environment, which therefore precluded a spatial study of turbulence due to the highly irregular shape of the underlying surface. Inagaki et al. (2013) and Morrison et al. (2017) recorded the TIR sequences at frequencies exceeding 30 Hz, but were focused on a smaller area of about 14.7 x 2.7 and 5 x 2 m^2, respectively. Evidently, the previous studies were impaired by low spatial coverage, insufficient temporal resolution, and disadvantageous positioning of the camera (oblique mounting close to the ground) – all of which are alleviated by the UAS survey performed in the present study.

In this work, we explore the capability of UAS thermal imagery for detecting variations in surface temperature at high spatial and temporal resolution. The specific goals are (1) to test the applicability of UAS TIR imagery for near-surface turbulence study and develop the necessary methodology to correct and analyze the images, (2) describe the time and length scales of the entire spectrum of surface temperature that is responsive to eddy impingement, with the focus on large structures, and (3) compare the UAS-based turbulence characteristics to those measured by ground-based sonic anemometry.

The work also demonstrates that the nadir thermal imagery used here can enable inquiry into the particularities of the coherent structures' evolution and movement derived from their 2D surface thermal traces. A 2-day field experiment over a pristine boreal peatland complex in Southern Finland was conducted using a thermal/RGB camera DJI Zenmuse XT2 mounted on a DJI Matrice 210 v2 quadcopter UAS. This site was selected for two pragmatic reasons: the presence of short low thermal inertia vegetation so as to minimize the so-called 'honami' effect, and due to the availability of eddy-covariance (EC) tower measurements and high frequency meteorological data.

2 Materials and methods

2.1 Thermal imaging by the UAS

The principal sensor used was a thermal/RGB camera DJI Zenmuse XT2 mounted on a DJI Matrice 210 v2 quadcopter (Fig. 1). The IR sensor of Zenmuse XT2, FLIR Tau 2 (FLIR Systems Inc.), had a resolution of 640 x 512 pixels, view angle of 45˚ x 37˚ with a 13 mm lens, thermal resolution of <0.05 K, and a maximum sampling frequency of 30 Hz.

Retrieval of IR videos were conducted in four flights near noon, two on 6 August and two on 28 August 2019 at a pristine boreal peatland complex Siikaneva, Southern Finland. Clear sky conditions prevailed during all four flights. About 5 min warmup time was allowed between UAS power on and takeoff as longer warmup is impractical considering the limited battery life. In each flight, the drone hovered above the EC tower at an altitude of 500 m, and was able to automatically maintain the position quite well irrespective of the wind conditions. However, the drone rotation was not as successfully controlled so the drone tended to slowly turn clockwise while hovering, which required manual correction throughout the flight.

https://doi.org/10.5194/amt-2020-382
Preprint. Discussion started: 26 October 2020

Atmospheric Measurement Techniques Discussions

The first three TIR video retrievals lasted for about 20 min, recording at 30 Hz (Table 1), whereas the last retrieval was cut down to 10 min due to an unexpected gimbal malfunction. The longest possible hovering flight time of 20 min at a 500 m altitude matches the producer's estimate of battery life as including a few minutes needed to rise and descend adds up to a total flight time of about 26 minutes. A TIR sequence of such a length thus approaches the conventional 30 min averaging period for computing turbulence statistics and vertical heat fluxes from ground-based sonic anemometry. Immediately before each flight, a non-uniformity correction was performed. This correction introduces large step-changes in the measured temperature field, which are non-uniform across the image. It was not applied again during the flight as this would have been detrimental for the detection of frame-to-frame temperature differences at high spatial and temporal resolution.,. To synchronize the drone thermal video with local time, a reference signal was created in each flight by quickly moving a 20x60 cm aluminum sheet which otherwise lied static on the ground. This manipulation was easily visible in the thermal sequences from a 500 m altitude. In each flight, the Zenmuse XT2 camera recorded surface temperature at the frequency of 30 Hz, producing about 20 Gb of raw data in FLIR file format. The sequences were therefore downsampled to 1 Hz as a means of reducing data set size and processing times, while preserving the relevant turbulent timescales. The surface emissivity was set to a constant 0.98, as the actual emissivities of the peatland surface constituents are not known; however they are expected to be close to 0.98 as a representative value of a moss-dominated boreal ecosystem emissivity (Antti-Jussi Kieloaho, personal communication). Before further analyses, the sequences were converted into Matlab® data arrays (.mat) using the FLIR ResearchIR® software; Matlab® was used for further data processing.

Figure 1. The UAS consisting of a drone DJI Matrice 210 v2 and a thermal/RGB camera DJI Zenmuse XT2.

Table 1. Flight metadata.

Date	Altitude	Start time	End time	Total duration	Frame count (at 1 Hz)
06 Aug 2019	500 m	12:28:54	12:47:58	19 min 4 s	1144
06 Aug 2019	500 m	13:28:35	13:47:17	18 min 42 s	1122
28 Aug 2019	500 m	11:22:24	11:42:16	19 min 52 s	1193
28 Aug 2019	500 m	12:23:09	12:33:36	10 min 27 s	629

2.2 Data post-processing

The data post-processing workflow presented in Fig. 2 consists of sequential steps from handling the raw sequences to inferring the impingement of turbulent motions from surface temperature data. The Steps 1–4 are common for all UAS-based thermal video surveys, while the Steps 5–6 are related to the specific study aim of retrieving turbulence characteristics.

https://doi.org/10.5194/amt-2020-382
Preprint. Discussion started: 26 October 2020

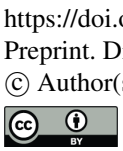

Atmospheric Measurement Techniques Discussions

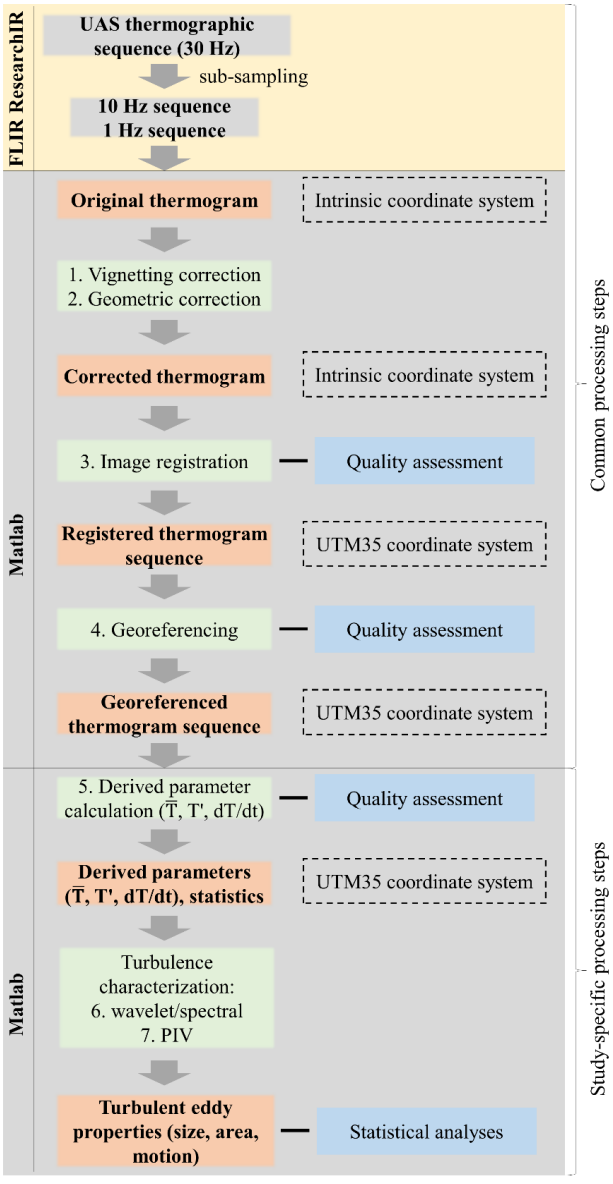

Figure 2. Data processing workflow.

2.2.1 Vignetting correction

The vignetting effect is the artificial reduction in brightness temperature towards the corners of the image, resulting from the difference of the lens transmissivity in the corners compared to the center. A method to define this lens-specific artifact and remove the effect from each image was developed. Before each flight, an image was taken of a plane fabric surface painted black to serve as a homogeneous temperature field. The reduction in temperature in the corners *versus* the center region of this thermogram (100 x 100 pixels) was found to exceed 2 ˚K. While the effect proved to be non-symmetrical, it was well described by a 4th degree polynomial surface fit (Appendix A).

2.2.2 Geometric calibration

https://doi.org/10.5194/amt-2020-382
Preprint. Discussion started: 26 October 2020


Atmospheric Measurement Techniques Discussions

A practical approach was developed for geometric calibration of the TIR camera. A checkerboard similar to what is commonly used for RGB camera calibration was constructed using 5 cm paper squares glued onto an aluminum plate (see Appendix B). The aluminum plate was heated up on a stove to increase the contrast between the high-emissivity paper checkers and the low-emissivity aluminum checkers. A set of 28 images of the checkerboard taken at different angles and distances was fed to the Matlab® Camera Calibrator tool, which produced the camera intrinsic parameters (Appendix B).

2.2.3 Image registration

Because of the rotation and translation of UAS during the TIR retrievals, the images needed to be co-registered, i.e. rotated and translated so a common coordinate system to match each frame in the video sequence. The first frame of each of the four TIR sequences was selected as a reference, with all the subsequent frames being co-registered with it. A satisfactory solution was achieved using the intensity-based approach by means of *imregister* Matlab® function, with the method set to OnePlusOneEvolutionary, metric MatthesMutualInformation, maximum iterations = 300, and initial radius = 0.001. The quality of registration was evaluated for the pairs i^{th} image – reference image using Structural Similarity Index (SSI), RMSE and signal-to-noise ratio (SNR) as metrics. When the registration algorithm failed to converge (typically only a few images per flight), the three metrics displayed either a downward peak (SSI, SNR) or an upward peak (RMSE) (not shown). In this case, the i^{th} image that could not be registered was replaced by the $i\text{-}1^{st}$ image.

2.2.4 Georeferencing

The registered images were georeferenced in order to relate them to the EC tower and to the georeferenced UAS RGB photo. To do that, four ground control points (GCP) were installed using 2 x 2 m cross-shaped aluminum targets with arms 20 cm wide on the ground. The GCPs formed an irregular quadrilateral centered at the EC tower, with the corners at approximately 100 m distance from the tower. The coordinates of GCPs were measured using a smartphone GPS antenna Trimble Catalyst DA1. At a 500 m altitude, one pixel of a thermal image at the given resolution and focal length is about 0.6x0.6 m at the image center, leading to the width of the crosses' arms being less than one pixel; the GCP was therefore determined by searching for the pixel with the lowest temperature within small (ca. 10 m across) regions of interest around the expected target location. As aluminum has significantly lower emissivity (0.03–0.05) than the peatland surface (~0.98), the contrast in TIR images was strong and GCP can be conveniently located thereby enabling georeferencing with a small root-mean-squared error (Appendix C).

2.2.5 Derived parameters, averaging and notation

The Cartesian coordinates used are (*x, y, z*) with x being the longitudinal (or along mean wind) direction, *y* being lateral, and *z* being the vertical direction with *z*=0 being the ground. The three instantaneous velocity components (*u, v, w*) are aligned along the *x, y, z*, respectively. Because the work here uses different averaging procedures including time (e.g. variables sampled at the EC tower), space, and space-time, the following conventions are used to indicate the averaging operators for an arbitrary flow variable χ evolving in space (*x,y*) and time (*t*). Time averaging (taken over the flight duration) at a given location (*x,y*) is indicated by overline $\bar{\chi}$ and deviations from time averaged quantities are indicated by primes so that $\chi(x,y,t) = \bar{\chi}(x,y) + \chi'(x,y,t)$. Spatial averaging (over the sampled image domain) at a given *t* is indicated by brackets $\langle\chi\rangle$ and deviations from this spatial average are indicated by double primes so that $\chi(x,y,t) = \langle\chi\rangle(t) + \chi''(x,y,t)$. Space-time averaging (over the image domain and flight duration) is indicated by a hat $\hat{\chi}$ and deviations from this space-time average are indicated by a tilde so that $\chi(x,y,t) = \hat{\chi} + \tilde{\chi}(x,y,t)$. For the instantaneous georeferenced surface temperature field *T(x,y,t)*, a space-time average was applied so that $\tilde{T}(x,y,t) = \hat{T} - T(x,y,t)$. A time-averaging at each pixel location was then conducted to obtain $\bar{\tilde{T}}(x,y)$ so that T'(x,y,t) = $\tilde{T}(x,y,t) - \bar{\tilde{T}}(x,y)$. The above zeroing was necessary to minimize the artificial changes in recorded absolute temperature; the thermal sensor of Zenmuse XT2, FLIR Tau 2, is known to have a large

https://doi.org/10.5194/amt-2020-382
Preprint. Discussion started: 26 October 2020

Atmospheric Measurement Techniques Discussions

drift in temperature offset caused by changing environmental conditions or camera temperature (e.g. Dugdale et al 2019). Temperature fluctuation distributions (see Fig. 5 and discussion therein) revealed that the physically sound $T'(x,y,t)$ values were contained in the interval $-1.5<T'<1.5$ K, whereas the more extreme values are deemed to represent noise; The $T'(x,y,t)$ was therefore de-spiked using those threshold bounds. Additionally, the time derivative of surface temperature field ($=dT'(x,y,t)/dt$) was calculated using a forward difference of the $T'(x,y,t)$ field for consecutive frames multiplied by frame sampling frequency.

2.2.6 Characterizing turbulent eddy size and shape: Spectral and wavelet analysis

The post-processed $T'(x,y,t)$ are now used to characterize the boundary-layer eddies impinging on the surface. Their spectral properties are first featured, followed by the transport patterns (i.e. imprint of advection velocity of large coherent eddies), size and area. A comparison between space-time surface temperature and high frequency air temperature measured at the EC location are conducted. Last, implications of $T'(x,y,t)$ to the determination of sensible heat flux from modified flux-variance similarity are discussed. Power spectra of $T'(x,y,t)$ were derived from both the drone maps and the EC-based sonic temperature. The power spectra were calculated in both the temporal and 2D spatial domains using Fast Fourier Transform.

Additionally, we used wavelet transform to infer 2D power spectra (Matlab® Wavelet Analysis Toolbox) and segregate the individual large coherent structures. Mexican Hat wavelet was applied to decompose the sequences at the spatial scales of 1-50 m. 2D wavelet transform was then applied to the $T'(x,y,t)$ sequences to characterize the larger coherent turbulent structures in the following manner. The 14 m scale was chosen for this particular purpose based on visual evaluation of how well the large coherent structure boundary was delineated; transform at this scale yielded isolated regions that best matched the most pronounced thermal traces. After 2D wavelet transform was applied to each image of the $T'(x,y,t)$ sequences, the pixels with wavelet powers smaller than -3.5 or greater than 3.5 were set to NaN to enhance the contrast between the positive and negative wavelet power regions. The positive and negative regions remaining after that filtering operation represent, in essence, the smoothed boundaries of the larger coherent structure thermal traces. The wavelet transform image was discretized by setting positive regions to 1 and those negative to -1, after which labeling by watershed transform. The labeled regions were then filtered by area (restricted to 500-50000 m^2) and mean absolute value of $T'(x,y,t)$ within their boundaries (must be >0.06 ˚K). Finally, the Matlab function *regionprops* was applied to extract the minor axis, major axis, orientation, area and the mean $T'(x,y,t)$ of each region. The regions now represent the boundaries of large coherent structures. These operations were performed on each image of the 1 Hz $T'(x,y,t)$ sequences; Fig. 3 gives a visual example of the above operations.

Another approach to spectral analysis was taken by calculating the spatial FFT spectra. To do so, each image was first rotated so as to make rows aligned with the anemometer WD averaged within ± 30 s of the image's time stamp. Then, the spectra were calculated for the rows and columns and averaged, yielding the along- and cross- wind spectra, respectively. The rows and columns containing less than 300 1 m values after rotation were omitted from the calculation.

https://doi.org/10.5194/amt-2020-382
Preprint. Discussion started: 26 October 2020

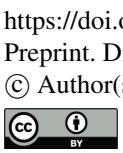

Atmospheric Measurement Techniques Discussions

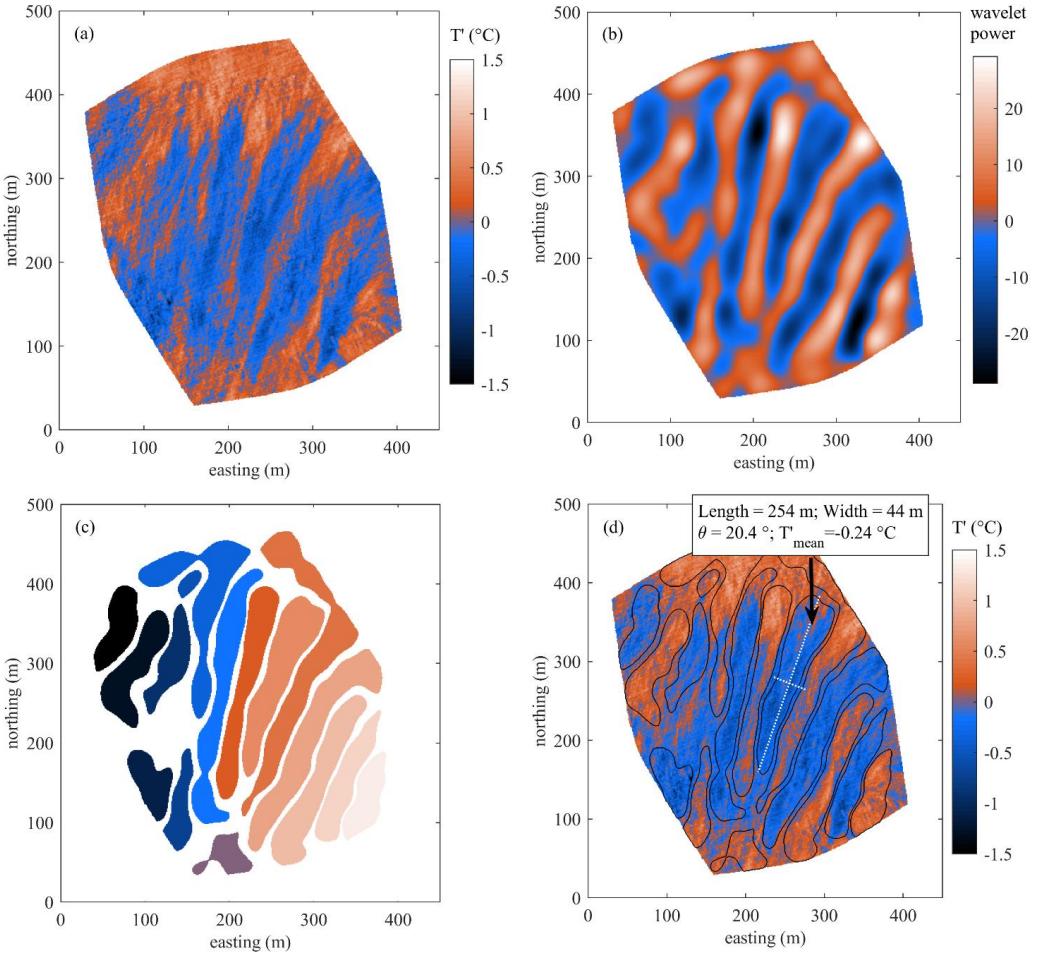

Figure 3. Large coherent structure identification method. (a): original georeferenced T'(x,y,t) image, (b): 2D wavelet transform at 14 m scale, (c): labelled coherent structure thermal imprints obtained by watershed transform of (b), (d): original T'(x,y,t) image (a) shown with the coherent structure boundaries from (c) and detailed information shown for one of the identified structures (length, width, clockwise rotation from the vertical and mean temperature excursion within the boundary).

2.2.7 Characterizing turbulent eddy advection velocity: Particle Image Velocimetry

An open-source particle image velocimetry (PIV) tool PIVlab (Thielicke and Stamhuis 2014) was used to derive the speed and direction of the coherent structures motion. PIV processing was performed on the T' maps wavelet-transformed at the scale of 5 m, which provided the necessary denoising. PIV yielded the horizontal velocity vector field of the coherent turbulent structure motions, from which the image-average advection velocity and direction were also derived. The background component of the images was removed using a built-in PIVlab GUI. After a series of tests, the following settings were chosen: interrogation area: 100 pix; step: 50 pix, subpixel estimation method: Gauss 2x3, correlation quality: extreme, autocorrelation disabled.

2.3 Ground-based measurements

Turbulent wind components and sonic temperature, as well as incoming global radiation and air humidity and temperature were measured on the EC tower (61°49'57.324" N, 24°11'34.116" E) that is part of the Siikaneva fen ecosystem monitoring station. The sonic anemometer Metek USA-1 mounted on a mast at a height of 3 m above the ground surface recorded the

https://doi.org/10.5194/amt-2020-382
Preprint. Discussion started: 26 October 2020

Atmospheric Measurement Techniques Discussions

three velocity components (u, v, w) and the sonic temperature T_s at a frequency of 10 Hz. The instantaneous wind speed WS and wind direction (WD) were calculated from these measurements as well as the mean WS and WD during each flight. The friction velocity u_*, the Obukhov length L_O and the roughness length z_0 were calculated using standard equations (Stull, 1988). The flux footprints were calculated for each flight after Kormann and Meixner (2001) (for details see Alekseychik et al. 2017b). The footprints were calculated using data partitioned into 5 min intervals.

3 Results

3.1 Micrometeorological conditions during the flights

The thermographic retrievals were conducted around noon on two cloud-free August days in 2019, but there turned out to be a fair amount of difference in meteorological conditions. The first day (6 Aug) was characterized by substantially higher instability and light winds, whereas 28 Aug showed more near-neutral conditions and higher wind speeds (Table 2). While the stability parameter estimated from 3 m EC data pointed at near-neutrality on 28 Aug, the higher wind speed and friction velocity indicate a predominantly mechanical or shear-induced PBL turbulence production, as opposed to 6 Aug when the PBL turbulence was more buoyancy-produced. August is generally the time of the seasonal peak in sedge biomass, leading to the annual peak in z_0 values (for z_0 investigation at this site, see Alekseychik et al. 2017a); the variation in stability explains the observation of higher z_0 on 6 Aug. The kinematic sensible heat flux $\overline{w'T'_s}$ was slightly higher on 6 Aug. The mean wind speed and direction obtained by PIV are similar to the anemometric observations.

Table 2. Summary of the mean micrometeorological parameters determined at the EC station, where σ_χ indicates the standard deviation of an arbitrary flow variable χ.

	Aver. period (min)	**WS (ms^{-1})**	**WD (°)**	**L_O (m)**	**u_* (ms^{-1})**	**z_0 (m)**	**$\overline{w'T'_s}$ (Kms^{-1})**	**σ_w (ms^{-1})**	**σ_{Ts} (K)**	**$z\ L_O^{-1}$**
6 Aug, flight 1	19.05	2.15	63	-10	0.24	0.15	0.100	0.34	0.64	-0.29
6 Aug, flight 2	18.68	2.00	65	-6	0.20	0.14	0.116	0.34	0.67	-0.54
28 Aug, flight 3	19.87	3.47	202	-47	0.39	0.10	0.092	0.44	0.49	-0.06
28 Aug, flight 4	10.45	3.67	213	-36	0.35	0.06	0.087	0.41	0.51	-0.08

3.2 Mean temperature field

https://doi.org/10.5194/amt-2020-382
Preprint. Discussion started: 26 October 2020

Atmospheric Measurement Techniques Discussions

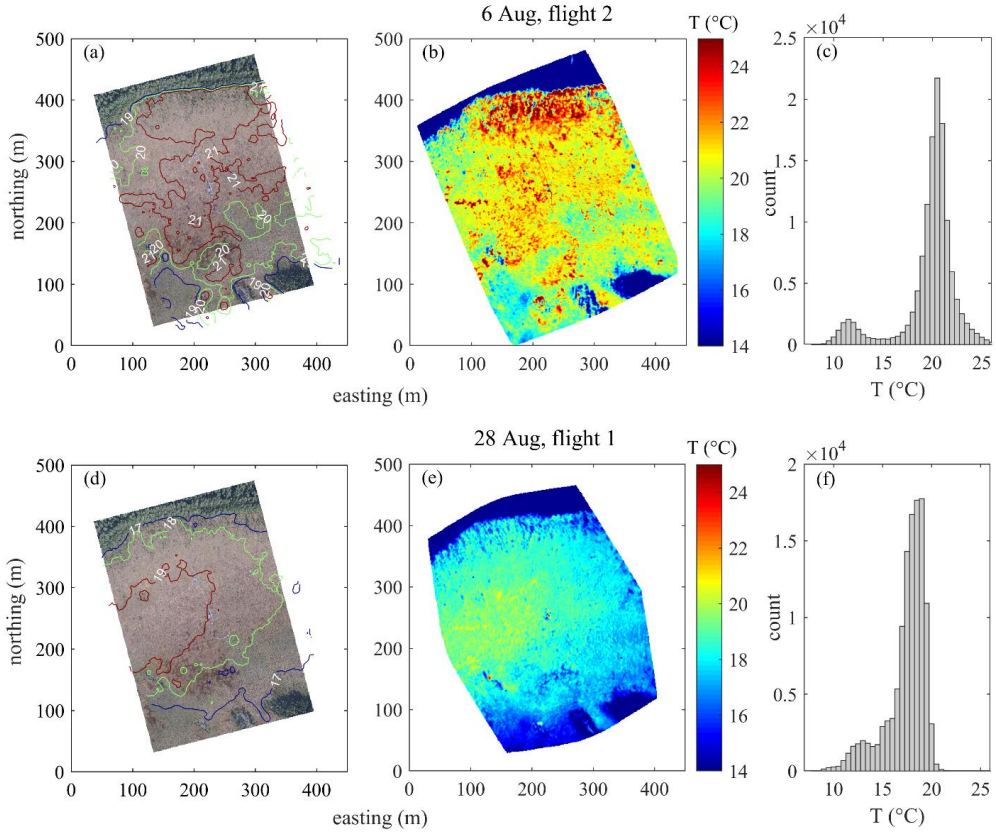

Figure 4. Pixel-mean surface temperature ($\bar{\bar{T}}(x,y)$) measured by UAS-mounted thermal camera for second flight of 6 Aug (a-c) and first flight of 28 Aug (d-f). The surface emissivity was assumed uniform at 98%. (a, d) RGB photographs with temperature isolines based on the calculated $\bar{T}(x,y)$; (b, e) surface temperature averaged for all frames of a flight ($\bar{\bar{T}}(x,y)$); (c, f) histograms of $\bar{\bar{T}}(x,y)$ shown in (b, e).

Fig. 4 summarizes the mean temperature variations observed on the two measurement days. Because of high similarity between $\bar{T}(x,y)$ of the flight pairs on both measurement days, only the flight 2 of 6 Aug and flight 1 of 28 Aug are shown. In terms of mean temperature, the tree stands and open peatland form two distinct regions with the tree stands appearing overall cooler and the peatland surface warmer (Fig. 4 c, f). Owing to the lack of detailed measurements on the emissivity differences between the two surface covers, a constant emissivity of 0.98 was applied to each pixel, which might have introduced some bias in the absolute temperature values. Nevertheless, the present data appear sufficient to note the broad surface temperature variations (in excess of 10 ˚C) in the open peatland on the two sampling days. The overall mean TIR temperature ($\bar{\bar{T}}(x,y)$ averaged over all pixels) was higher on the 6 Aug (20.5 ˚C) than on 28 Aug (18.0 ˚C), which is evident from Fig. 4 (b, e). Secondly, $\bar{T}(x,y)$ shows different spatial distributions. While on 28 Aug the highest temperatures are concentrated in a circular area in the western part of field of view (FOV), on 6 Aug an additional zone of high $\bar{T}(x,y)$ is observed near the northern forest edge (see the isolines in a, d). The peatland drainage area in the lower third of the image is characterized by the lower temperatures, part of which is formed by extensive hollow complex recognizable by its dark colour in the RGB image.

Small-scale $\bar{T}(x,y)$ variability is consistent with the hollow-hummock patterning of this ecosystem. The resulting $\bar{T}(x,y)$ patterning was intense on 6 Aug, with 17-20˚C in the hollows and 22-25˚C on the southern faces of the hummocks. The 28 Aug temperatures were rather homogenized, probably due to stronger wind, with hollows at about 18˚C and hummocks 20˚C.

https://doi.org/10.5194/amt-2020-382
Preprint. Discussion started: 26 October 2020

Atmospheric Measurement Techniques Discussions

The observed spatial patterns in $\bar{T}(x,y)$ are not artifacts of the camera, which was assured by (i) the absence of a temporal trend in the spatial distribution of temperature maxima and (ii) the absence of significant temporal trend in the mean temperature of the frame, which, if present, would have indicated the drift due to camera stabilization and change in camera body temperature as a result of WD, WS and T_a changes. That is to say, uncooled thermal camera measurements are always plagued by those artifacts, but in this case they were weak and did not distort the environmental signal.

3.3 Ground temperature fluctuations

Fig. 5 features the probability density function (PDF) of $T' = \bar{T}(x,y) - < \bar{T} >$ observed in each of the four flights. The analysis suggests that the PDF is near-Gaussian with some minor deviations at the tails. A small, but significant, difference is in the kurtosis of the distributions, or, in other words, the maximum amplitude of temperature fluctuation. Allowing for the instrumental and processing-related noise, we may adopt the 2nd and 98th percentiles as estimates of the minimum and maximum T'; on the open peatland surface, those correspond to fluctuations of ± 0.7 ˚C and ± 0.6 ˚C around the mean on 6 Aug 28 Aug, respectively. It is noteworthy that the surrounding coniferous forest always had a more fluctuating surface temperature that was about ± 1.0 ˚C and ± 0.8 ˚C on the respective days, reflecting the lower heat capacity of needles compared to peatland surface (not shown).

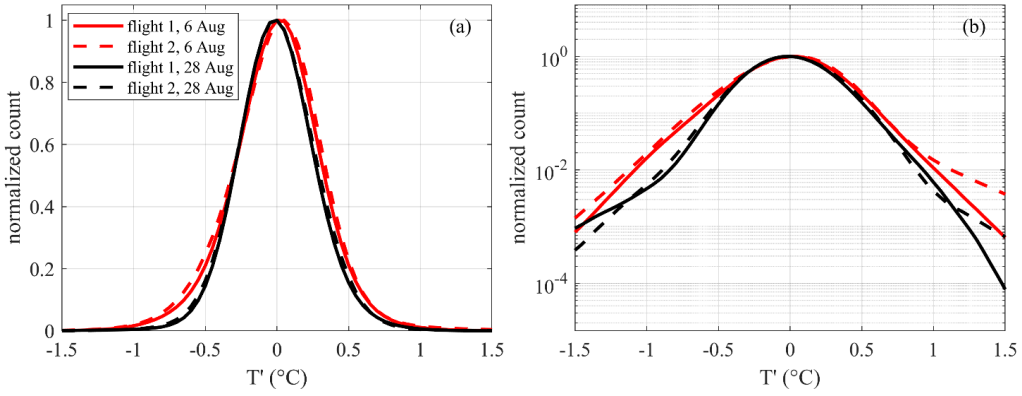

Figure 5. Normalized distributions of peatland surface temperature excursions during each flight, shown with linear (a) and logarithmic (b) y-axis.

The information provided in Fig. 5 is visualized spatially in Fig. 6. Not only the excursions of ground skin temperature are lower in the open peatland than in the other surfaces (rocky islands, tall tree stands along the S and N edges of the image), their standard deviation is similarly contrasting. The pattern in the open peatland appeared patchier on 6 Aug than on 28 Aug. On both days, however, $\sigma_{T'}$ showed large-scale spatial inhomogeneities: it formed faint but recognizable elongated regions of alternating low and high $\sigma_{T'}$ extending along the mean wind direction.

https://doi.org/10.5194/amt-2020-382
Preprint. Discussion started: 26 October 2020

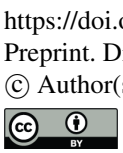

Atmospheric Measurement Techniques Discussions

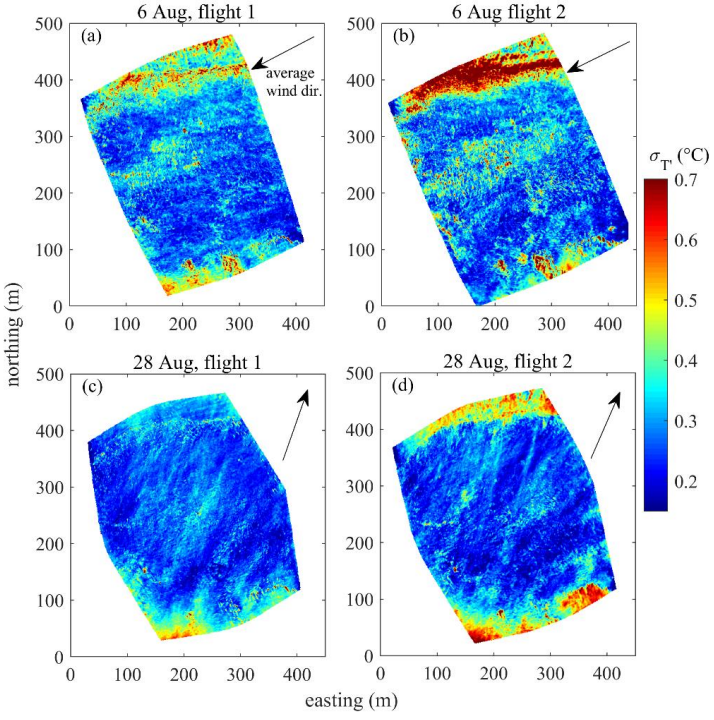

Figure 6. Maps of $\sigma_{T'}$. The arrows show the mean wind direction during the flight.

285

The average FFT spectra of the UAS T' (T_g'), representing average power at given frequency across the whole image, and sonic anemometer-based T_s spectrum are compared in Fig. 7. They exhibit the same canonical -5/3 inertial subrange slope until about 0.2 Hz, where the UAS spectrum starts flattening for two primary reasons, namely the thermal camera noise and a high thermal inertia of the wet moist moss surface dampening the thermal influence of the small eddies.

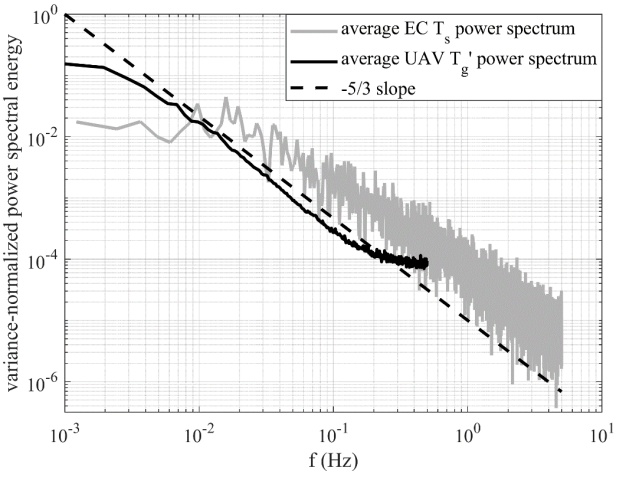

290

Figure 7. Normalized FFT power spectra of sonic temperature and drone temperature fluctuation. The UAS spectrum was calculated using 1 Hz data.

3.4 Detected turbulent structures and their characteristics

https://doi.org/10.5194/amt-2020-382
Preprint. Discussion started: 26 October 2020


Atmospheric Measurement Techniques Discussions

Distinct turbulent flow patterns were clearly visible in the temperature anomaly (T'(x,y,t)) videos (see the videos in the Supplement). Based on visual inspection, three major types of large-scale flow organization or super-structure could be distinguished (Fig. 8): 1) divergent or "fanning out" pattern, 2) quiescent period when multiple convergence/divergence zones could be observed across the FOV, and 3) elongated linear structures.

Both flights of 6 Aug yielded the evidence of flow structure cycling between the modes 1–2, with a time scale of 2–5 min. The fanning pattern (1), when at peak strength, occupied the entire FOV and resulted in strong divergent flow pattern on the scale of several hundred meters – the wind direction is occasionally seen to differ by over 45˚ within a single image (Fig. 8 a). The "fan" consists of elongated eddies ca. 20–100 in length and 10–30 m in width, causing moderate ground temperature anomalies. On one occasion during the 1st flight on 6 Aug, the initiation of a fanning pattern is seen as a concentrated leaf-shaped cold anomaly on the ground initially about 200 m in length, with the "rays" diverging from the stream-wise axis in nearly opposite directions and rapidly emanating outwards. After this initial sweep-like stage, when the ground T anomaly caused by the structure reaches -1 ˚K, a weaker and more persistent fanning pattern as in Fig. 8 (a) is initiated. The intermissions in the form of quiescent periods characterized by lower wind speeds and collapse of large-scale structure are demonstrated in Fig. 8 (b, c). The relatively small scale of the turbulent structures resulted in their being confined to the roughness sublayer and thus sensitive to large roughness changes, which may explain the well-pronounced wall effects near the forest edge (Fig. 8 a, b). An interesting feature is the onset of large sweeps seemingly dissociated from the mean near-surface flow, the most pronounced of which is displayed in Fig. 8 (c). The life cycle of this sweep was about 1 min from the time it reached the ground until the moment its thermal trace dissipated. Counter-flow motion of the cold structures, however less pronounced, could be detected two more times during the flights of 6 Aug.

To the contrary, the large-scale flow on 28 Aug was completely dominated by pattern type 3, persisting throughout the flight, without the periods of true quiescence as was the case on 6 Aug. At a maximum, the length of those structures could exceed the largest dimension of FOV (ca. 400 m), their width being 30–100 m, but judging from visual observation most structures never reached that size. The elongation of the linear structures seemed to be positively related to the periods of increased wind speed. Wall effects at the forest edge were virtually absent, implying significant vertical dimension of the impinging structures (at least substantially exceeding the roughness sublayer height above the forest stand, which is about 20 m tall).

https://doi.org/10.5194/amt-2020-382
Preprint. Discussion started: 26 October 2020

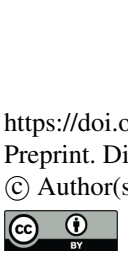

Atmospheric Measurement Techniques Discussions

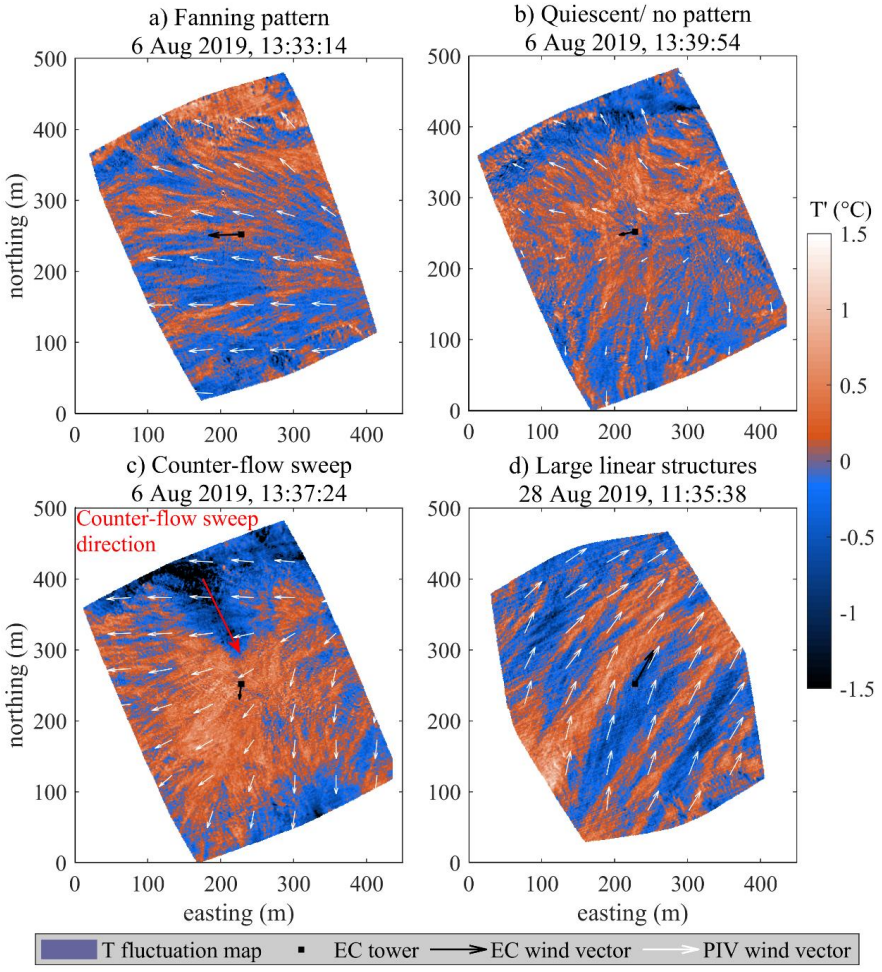

Figure 8. The typical cases of flow organization observed during the flights of 6th and 28th August 2019. The time stamps are given for the presented instantaneous T' snapshots, whereas the PIV calculations were performed using the data within ±40 s of those times. Wind vector scale is the same for each flight, PIV and EC; a twice longer vector is shown in (b) for ease of reading.

The above case studies also demonstrate the general feasibility of PIV for boundary layer flow analysis based on thermal data. Table 3 reports average wind parameters for the illustrated cases. Here, averaging over a period of 80 s centered on the image timestamp was applied so that to both cover the interval of stationary flow required for PIV processing, and account for the typical "life time" of large coherent structures. The average EC wind direction was within a few degrees of the average of four PIV vectors in the vicinity of the EC tower - in the cases when the flow was stationary within FOV (Fig. 8 a, b, d). In (c), where non-stationarity appears to be connected to the large counter-flow sweep that passed through the EC sensor, the PIV WD did not average as close to the EC WD. The EC signal seems to have been dominated by that sweep, while the PIV flow field was unaffected by this temporary disturbance. Another such event is seen in the very end of the second flight of 6 August (see the corresponding video). In terms of wind speed, there is a difference between spatially homogeneous and stationary flow field (a, d) and inhomogeneous/non-stationary flow (b, c): in the former, the EC WS was higher, in the latter, the two estimates were similar.

https://doi.org/10.5194/amt-2020-382
Preprint. Discussion started: 26 October 2020

Atmospheric Measurement Techniques Discussions

Table 3. Mean wind parameters for the cases in Fig. 8.

	PIV $\overline{U}$ (m s^{-1})	EC $\overline{U}$ (m s^{-1})	PIV WD (°)	EC WD (°)
Fig. 8 a	1.8	2.9	100	88
Fig. 8 b	0.8	0.7	82	78
Fig. 8 c	1.7	1.4	41	6
Fig. 8 d	2.4	3.5	201	208

The periodicity of the turbulent motions was further investigated by analyzing the continuous 2D wavelet transforms on the spatial scales of 1–50 m. The result is presented in the form of scalograms normalized by the means of the power at the respective scales in Fig. 9. From Fig. 9, it becomes evident that periods of intensified turbulence were more frequent on 28 August (flights 3–4) than on 6 August (flights 1–2). The normalized power generally varies more at the large spatial scales than on the small scales. A conspicuous feature is contributed by the periods of wavelet power strongly increased across the larger scales, waning somewhat in the lower scales. By comparison with the T' videos, one finds that they correspond to the events of strong flow which took the form of fanning events during the flights 1 and 2. The strong fanning event in the beginning of flight 2 left a particularly sharp signature (Fig. 9 b). The waves of elongated parallel structures during the flights 3 and 4 left a similar signature, but had shorter time spans in accordance with their lifespan. However, another interesting signature also emerges: an isolated region of increased power that only encompasses a narrow range of scales. Three such "scale-dependent" bursts may be seen during flight 3, around t = [400, 650, 750] s (Fig. 9 c).

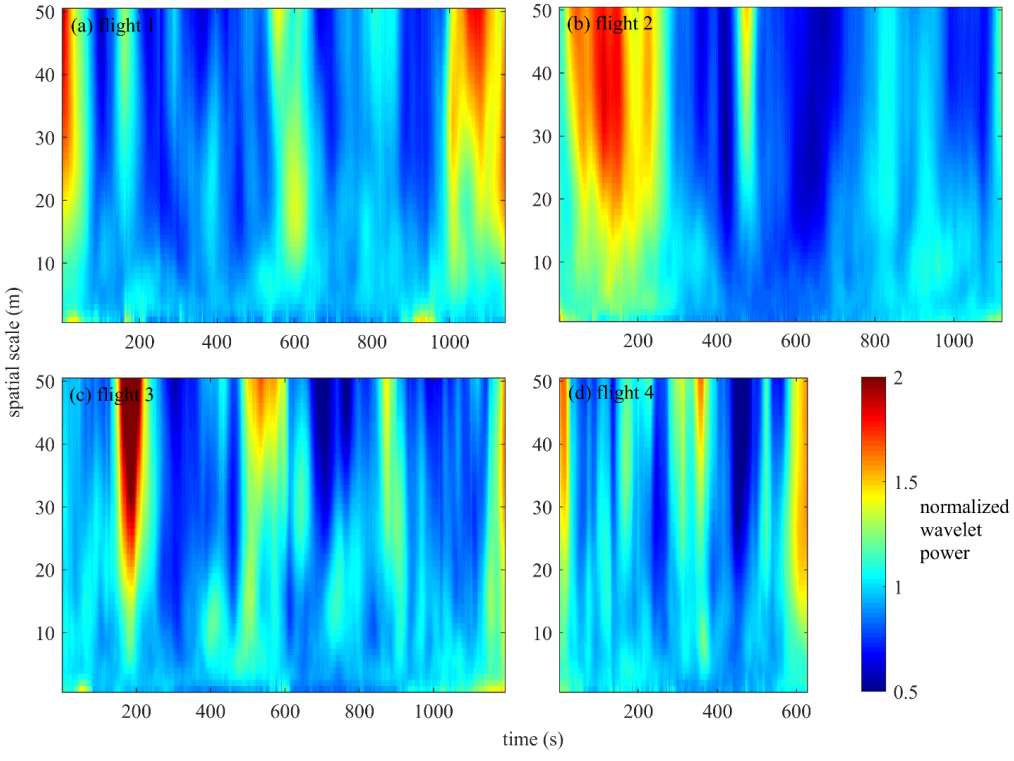

https://doi.org/10.5194/amt-2020-382
Preprint. Discussion started: 26 October 2020

Atmospheric Measurement Techniques Discussions

Figure 9. Scalograms of 2D continuous wavelet transforms on the spatial scales of 1–50 m. Absolute values of wavelet power are taken in order to average over the negative and positive *T* excursions, and normalized by the average absolute power at the respective scale.

The spectral properties of the ground temperature fluctuations were additionally explored by inquiry into their along- and cross-wind spectra. Now, each T'(x, y, t) image was rotated and interpolated on a rectangular grid to direct the mean wind along the x-axis, y-axis being a cross-wind coordinate. The wind direction used to perform this rotation was calculated as the average anemometer WD for the period of ±30 s around the timestamp of an image. FFT power spectra were calculated for rows and columns of the rotated images on the scales of 2–128 m, and averaged, providing the mean along- and cross-wind spatial power spectra. Rows and columns left with less than 300 pixels after rotation were excluded as unrepresentative of the largest spatial scales.

Two metrics are used to describe the relations between the fluctuations on different spatial scales and the along and cross wind directions, namely, (i) ratio between the spectral powers at 128 and 10 m for both along- and cross-wind directions, and (ii) ratio between the along-wind power at 128 m to cross-wind power at 128 m. (i) can be interpreted as a measure of domination of large coherent structures at a given time, and also as a measure of anisotropy when the ratios for along- and cross-wind directions are compared. While (ii), too, is a measure of anisotropy, it is directly related to the largest captured scale of 128 m. The two metrics are plotted in Fig. 10.

Most obvious is the striking dissociation between the along-wind and cross-wind ratios of the 128 m / 10 m spectral power (metric (i)), and their intense individual variability. Generally, for both directions, the periods of increased ratios (i) correspond to the periods of intensified ground temperature fluctuations highlighted in Fig. 9, while the opposite is true for the quiescent periods as seen in Fig. 9. The tallest peaks reach about 80, indicating the total dominance of large-scale coherent structures over smaller-scale near-ground turbulence. Most of the time, the ratios for the along- and cross-wind directions are anti-correlated in the sense that typically only one of the two may peak at any given time. For example, the pronounced coherent events detected earlier at the end of flight 1, beginning of flight 2 and during flight 3 are associated with a peaking 128/10 m power ratio, indicating the contact of large coherent structures with the ground at those times. However, during flight 3 the highest values are attained by the along-wind 128/10 m power ratio, in contrast to the first two flights where the cross-wind ratio was higher.

The ratio of the 128 m spectral powers (metric ii) attains the values of 0.2–5 and displays different dynamics during the flights 1–2 and 3, being generally below unity in the former case and more often above unity in the latter case. It should be noted that the periods of increased metric (i) for cross-wind direction generally correspond to the troughs in metric (ii), as both require the cross-wind spectral power at 128 m scale to be high.

https://doi.org/10.5194/amt-2020-382
Preprint. Discussion started: 26 October 2020

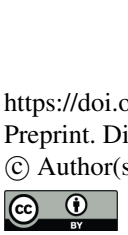

Atmospheric Measurement Techniques Discussions

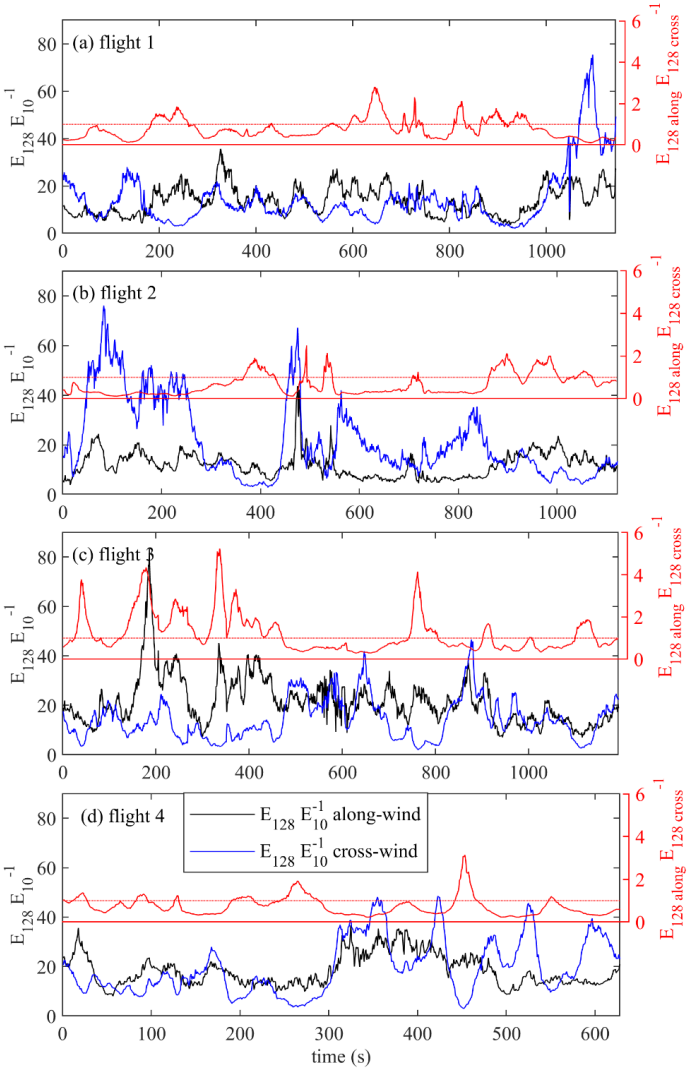

Figure 10. The ratio between the FFT spectral powers at the scales of 128 m to 10 m for the along- and cross-wind directions (black and blue lines, respectively) and the along- to cross- wind spectral power ratio at the scale of 128 m (red lines).

3.5.1 Eddy size and shape derived from 2D wavelet transforms

The eddy sizes and shapes extracted from the 2D wavelet transform are shown in Fig. 11. The algorithm (Sect. 2.2.6 and Fig. 3) detected typically 5–20 eddies per image, the eddy sizes varying between 70–240 m in length and 20–80 m in width and having areas of 1000-8000 m^2 (see Fig. 3 d for an example of the derived eddy parameters). The eddy parameter distributions are roughly Gaussian and display a modest but significant progression of the median eddy dimensions and area in the flight order 2–1–4–3. The flights 1–2 group close together, flight 4 being moderately different, whereas the flight 3 stands more separate. In flight 3, the detected major axes were longer while the minor axes were shorter, providing for the highest eddy length/width ratio of all flights. The eddy areas observed during that flight were generally the largest, as well.

The orientation of the eddies also corresponded well to the wind speed averaged over 1 min interval centered on the thermogram record time (not shown). The thermogram-derived 14 m scale eddy directions, however, show a systematic 0-20˚ clockwise rotation relative to the anemometer wind, in all four flights, which we cannot explain. The elongation of eddies

https://doi.org/10.5194/amt-2020-382
Preprint. Discussion started: 26 October 2020

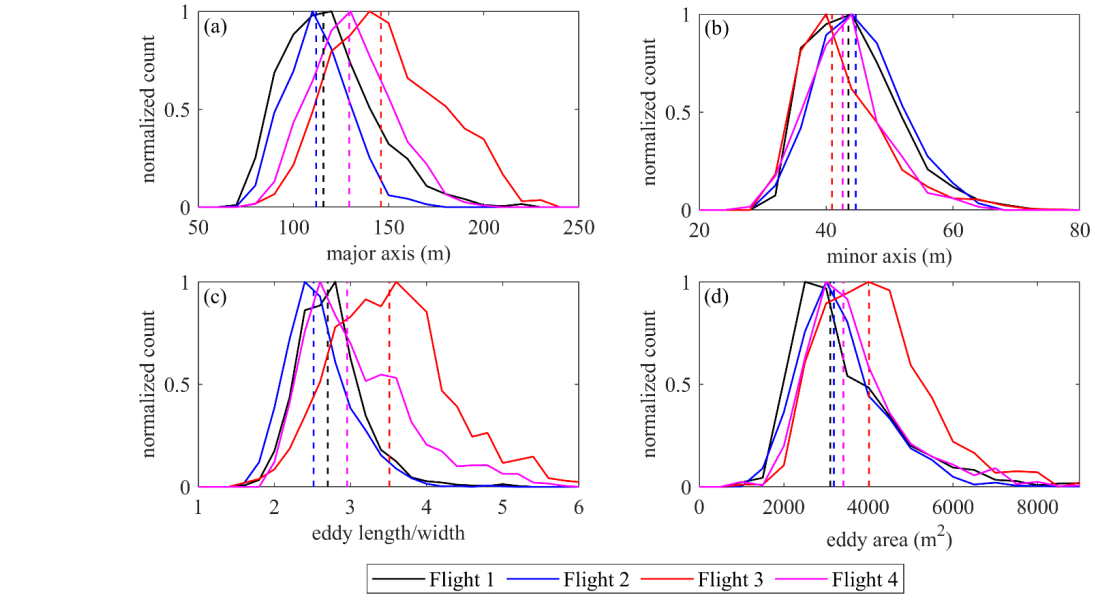

Figure 11. Distributions of size parameters of the eddy thermal traces derived from the 2D wavelet transforms. The vertical dash lines mark the distribution medians.

The relationship between the 5-min average eddy properties (size and shape) and diabatic stability ($z\,L_O^{-1}$) and u_* is shown in Fig. 12 (a–d). Eddy length to width ratio is in positive correlation with both quantities (Fig. 12 a–b), implying the residence of more elongated coherent structures during the periods of lower instability and intensified mixing. The relationship between eddy area and $z\,L_O^{-1}$ and u_* (Fig. 11 c–d) is less strong. Eddy length/width ratio is also positively correlated with eddy area (Fig. 12 e) meaning large eddies are typically elongated along the mean wind. The data in Fig. 12 are shown partitioned into warm and cool eddies to examine the possible differences; the offsets between the eddies of different signs reach 10–15% in relative but fail to form a clear trend against u* or stability.

https://doi.org/10.5194/amt-2020-382
Preprint. Discussion started: 26 October 2020

Atmospheric Measurement Techniques Discussions

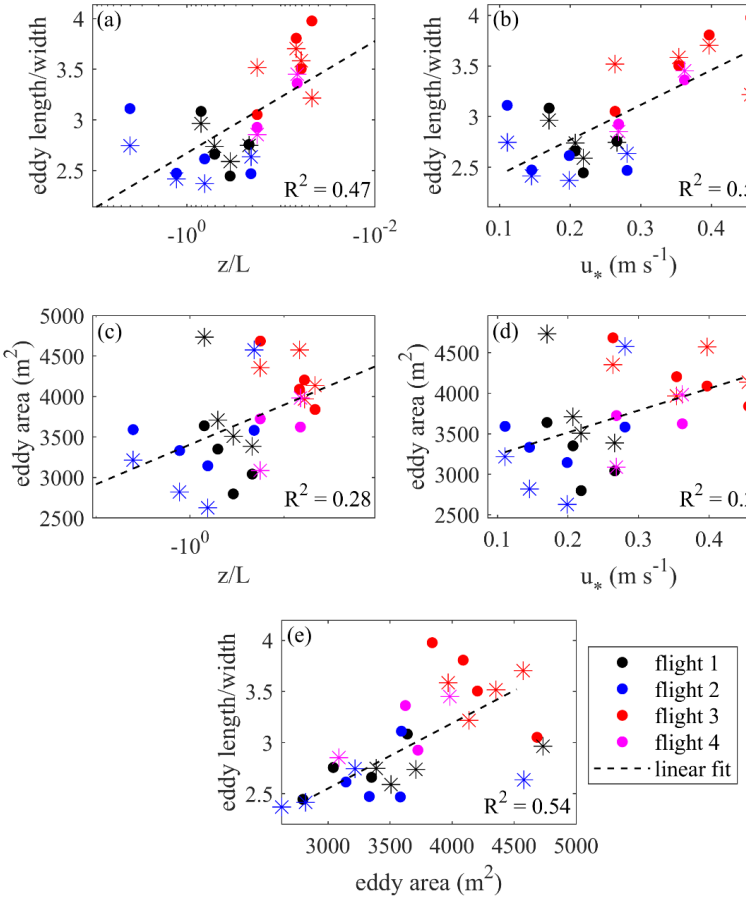

415

Figure 12. (a–d): Relation between the 5-min average properties of eddy thermal traces (mean area, length to width ratio) and the corresponding averages of z/L_O and u_*; (e) length to width ratio *versus* mean area. The * stand for eddy traces with positive mean T', ● for negative mean T'.

420 **3.5.2 Comparison of air and ground temperature excursions**

The drone and EC-derived quantities (σ_{Tg}, σ_{Ts} and mean T' difference between the positive and negative eddy regions $\Delta(T_g^-, T_g^+)$) were again averaged over 5-min periods to achieve a finer temporal resolution roughly matching the time scale of the coherent structures. First, we note that temperature fluctuations measured in the air and on the ground are clearly associated (Fig. 13); the statistics of ground temperature fluctuations show R^2 of 0.33-0.38 against the standard deviation of sonic
425 temperature. However, when removing 'outliers' marked with * and # in (b) and (c) the R2 increases up to 0.6. Upon checking with the previously identified chronology of the coherent events, we find that those 5-min periods that appear to be outliers were contemporaneous with the passage of major cool coherent structures in the beginning of the flights 2 and 3 (see Fig. 9).

https://doi.org/10.5194/amt-2020-382
Preprint. Discussion started: 26 October 2020

Atmospheric Measurement Techniques Discussions

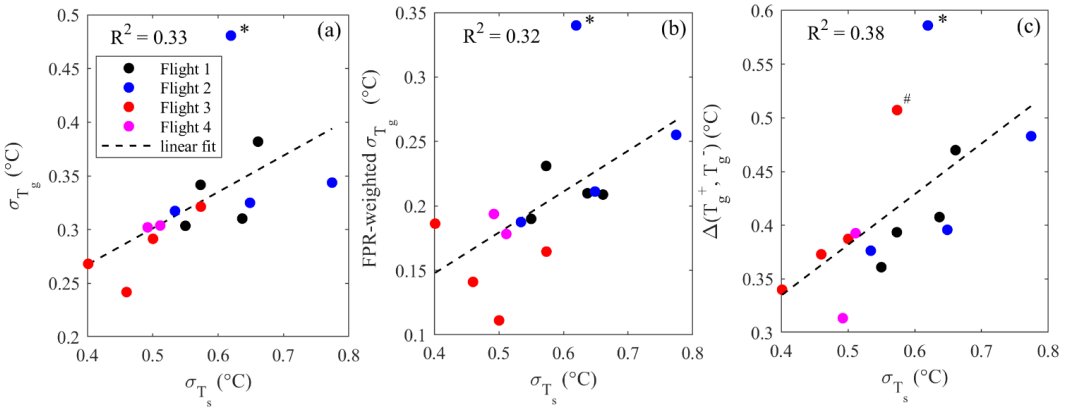

Figure 13. Drone data (a – STD(T), b – EC footprint weighted STD(T), c – difference between the mean temperature excursions in cold and warm eddy traces) against the standard deviation of sonic temperature. * and # indicate the outlying 5-min periods in the beginnings of the flights 2 and 3 when particularly strong coherent structures occurred.

Discussion

A UAS comprised of quadcopter DJI Matrice 210 V2 and camera DJI Zenmuse XT2 was capable of hovering at the altitude of 500 m for a maximum time of 20 minutes, as the camera continuously recorded surface temperature pointing at nadir. Such a setup was beneficial for the measurement of impingement of PBL turbulence on the surface: on the one hand, the record length approaches the typical averaging period of the ground-based eddy-covariance data, and was sufficient to analyze the periodicity of the large coherent turbulent structures forming in a summertime convective PBL over a peatland; on the other hand, the size of an area seen from 500 m height with a 13 mm lens was 420 x 335 m, large enough to fit in the largest thermal structures. With these dimensions, the requirement that FOV should be bigger than the integral length scale of turbulence, proposed by Christen et al. (2012), is met. A nadir direction of view also resulted in a uniform thermal resolution at the surface of about 0.6 m/pix, which was high enough to resolve the small eddies. Therefore, the present TIR study has a number of advantages over the prior work in four ways: (a) the surveyed area is the largest, (b) the camera was aimed at nadir, minimizing the geometric distortion across the thermogram; (c) the 10 Hz record rate is sufficient to resolve some of the inertial-scale turbulent eddies, (d) the UAS platform could be positioned at an arbitrary point in space and thus can be positioned to overlap with the footprint of the other surface flux measuring apparatus such as the eddy-covariance station in this case. Thus, this is the first successful attempt to use a drone to explore a wide spectrum of eddy sizes impinging on the surface via TIR imaging. The current image analysis approach to identify turbulent coherent structures has the significant advantage over analyzing fixed sensor data on atmospheric state variables ("1D approach" in the following) in that the structures have a distinct appearance that is readily recognizable with naked eye or by automated algorithms.

A problem inherent to the traditional fixed-sensor meteorological observation is that the center of a coherent structure might pass at any distance from the sensor, thus making the "slice" observed in the recorded time series an unreliable representation of temperature fluctuation caused by the actual structure. In contrast, 2D imaging allows for identification of the turbulent structure shape (from its fingerprint on the ground), and its position relative to ground at any moment in time. However, even experiments employing 2D thermal imagery tended, in the past (Christen et al. 2012, Garai and Kleissl 2011, Inagaki et al. 2013), to drift towards a "statistical" perception of the coherent structures, forgoing all the potential to get a hold on the actual geometry and movement of the individual structures offered by 2D TIR. Furthermore, a 1D approach relies on turbulence being ergodic, as a result, precluding the segregation of non-stationary events from the mean flow, such as the counter-flow event in Fig. 8 (c); such non-stationarities have not been addressed in the previous studies either. This study attempted to avoid these pitfalls by focusing on spatiotemporal analyses.

https://doi.org/10.5194/amt-2020-382
Preprint. Discussion started: 26 October 2020


Atmospheric Measurement Techniques Discussions

The assumption underlying our approach to the imaging of turbulence is that the coherent structures dominating the surface layer flow, such as thermals, hairpins, and roll vortices remain attached to the ground for a period long enough for their evolution to be described, and this attachment is sufficiently "tight" to provide information on their internal structure. This assumption finds support in the similarity of the structures observed in this UAS experiment to those found earlier in a plethora of studies employing DNS (Fang and Porté-Agel 2015, Laima et al. 2020), Doppler radar (Newsom et al. 2008), PIV (Inagaki et al. 2013) and other methods.

The 2D organization of PBL turbulence was also very disparate on the two field days. Given the difference in meteorological conditions and micrometeorological parameters, one might expect some difference in the organization of turbulence, and much evidence has emerged in this study to support this view. It appears that the conditions of 28 August, characterized by smaller instability but more intensive mixing due to stronger wind on 6 August (Table 2), led to the formation of larger and more elongated coherent structures (Figs. 8, 11). Contrastingly, when the wind picked up on the 6 August, the dominant large-scale structure was a field of smaller eddies diverging in a fan-shaped manner. The mixing on 28 August was apparently contributed by shear stress and mechanical turbulence, whereas on 6 Aug it was rather controlled by buoyancy and convection, which we think is the primary reason for such a substantial difference in the large-scale ABL turbulence organization. The same driver is perhaps responsible for the slower development and longer survival of self-sustaining large- scale turbulent structures on the 6 August.

The coherent structures were aligned with the wind direction, which was shown independently by comparison between the anemometric data with flow directions obtained with the help of PIV (Fig. 8, Table 3) and the orientation of eddies detected by the 2D wavelet-based algorithm (Fig. 11). However, the PIV algorithm provided for a closer match with the EC wind by virtue of its relying on the small-scale turbulence, whereas the larger-scale structures whose orientation was calculated explicitly proved to deviate by 20° clockwise, and didn't follow the EC wind trend on the short timescale. The advection speed of the small-scale turbulence determined by PIV was also close to the EC wind speed.

The differences in periodicity and self-organization of turbulence on the two measurement days were assessed by spatial spectra in two ways, by 2D wavelet transform and cross- vs. along- wind FFT spectra. The 2D wavelet scalograms (Fig. 9) indicate transitions from high to low spectral power that are associated with impingement and dissipation of large coherent structures, which happened more frequently on the 28 August than 6 August. The two metrics constructed of cross- and along-wind FFT spectra (Fig. 10) support the periodicity and give a general indication that the periods of increased power in Fig. 10 were the times when large structures elongated along WD dominated.

The present study paves way to determination of surface sensible heat flux based on UAS thermal videos. Firstly, there are indications that the flux variance technique (Albertson et al. 1995) may be adapted to the calculation of sensible heat flux from UAS thermal videos. As shown in Fig. 12, the correlation between the standard deviations of sonic temperature and UAS temperature may be sufficiently high to parameterize σ_{Ts} as a function of σ_{Tg} and use it in the flux variance expression of Albertson et al. (1995). The data set of the present study is, however, too short to consistently verify the validity of the approach.. However, we propose that if the eddies are large, attached to the ground, and contribute most to heat transport – and the flow is ergodic – space-time mean σ_{Tg} of the eddy at the ground can be used to derive heat flux caused by the impingement of an eddy. Alternatively, a 'pixel' type flux variance can be used to infer variations in sensible heat flux, where heat flux is calculated for individual pixels using their specific σ_{Tg}. Secondly, the possibility to segregate large eddies and derive the durations of their contact with the ground enables the use of a modified surface renewal approach (Paw U et al. 1995), in which the amplitude of temperature excursion and period of an eddy are the drivers of heat flux.

Conclusions

The present study develops a framework for planetary boundary layer turbulence analysis based on UAS thermal camera measurements. The methods for thermal sequence retrieval, its postprocessing and detection of large coherent structures were

https://doi.org/10.5194/amt-2020-382
Preprint. Discussion started: 26 October 2020

Atmospheric Measurement Techniques Discussions

proposed. The performance and validity of the methods were tested in a case study over a flat and treeless boreal peatland in South Finland. The spectral and morphological analysis pointed at the domination of large coherent structures up to tens of meters in width and hundreds in length, as expected in a convective PBL. Wind parameters independently observed by ground-based eddy-covariance setup provided support to the turbulence statistics derived by thermal sequence analysis. However, the novel 2D approach of this study also allowed for detection of instationary events such as counter-flow sweeps, which is beyond the capacity of previous observational methods. Larger, longer and more linear eddies were associated with lower instability as expressed by the stability parameter $z\ L_O^{-1}$, while smaller and more circular eddies were observed at higher instability. The association between the surface temperature fluctuations on the ground and in the air, and the possibility to directly infer the residence time of an eddy and T fluctuation created by it, prepare ground for the application of sensible heat flux estimation by flux variance (Albertson et al. 1995) and surface renewal (Paw U et al. 1995) methods.

Appendix A: Details of the vignetting correction

The fourth-order polynomial descripting the vignetting effect (see Fig. A1) is described by:

$$S(x, y) = p_{0,0} + p_{1,0}*x + p_{0,1}*y + p_{2,0}*x^2 + p_{1,1}*x*y + p_{0,2}*y^2 + p_{3,0}*x^3 + p_{2,1}*x^2*y + p_{1,2}*x*y^2 + p_{0,3}*y^3 + p_{4,0}*x^4 + p_{3,1}*x^3*y + p_{2,2}*x^2*y^2 + p_{1,3}*x*y^3 + p_{0,4}*y^4 \quad (A1)$$

with x and y being the x and y- coordinate of an image pixel and $p_{i,j}$ the fit parameter value. The derived lens-specific coefficient values are given in Table A1.

Table A1. Coefficients of the 4th degree polynomial surface describing the vignetting effect.

Coefficient	value	95% CI
$p_{0,0}$	23.79	23.78, 23.79
$p_{1,0}$	0.02014	0.0201, 0.02019
$p_{0,1}$	0.01298	0.01292, 0.01303
$p_{2,0}$	-5.922e-05	-5.944e-05, -5.9e-05
$p_{1,1}$	-5.36e-05	-5.382e-05, -5.338e-05
$p_{0,2}$	-3.069e-05	-3.104e-05, -3.034e-05
$p_{3,0}$	8.734e-08	8.687e-08, 8.782e-08
$p_{2,1}$	8.291e-08	8.245e-08, 8.336e-08
$p_{1,2}$	9.391e-08	9.334e-08, 9.449e-08
$p_{0,3}$	2.667e-08	2.574e-08, 2.761e-08
$p_{4,0}$	-6.603e-11	-6.639e-11, -6.567e-11
$p_{3,1}$	-3.4e-12	-3.795e-12, -3.006e-12
$p_{2,2}$	-1.465e-10	-1.47e-10, -1.46e-10
$p_{1,3}$	4.615e-13	-1.547e-13, 1.078e-12
$p_{0,4}$	-2.202e-11	-2.29e-11, -2.114e-11
$p_{0,0}$	23.79	23.78, 23.79

The vignetting correction matrix was obtained by subtracting the polynomial fit from the mean temperature of the center. We assumed that vignetting is zero at the center and computed the mean temperature from of the 40x40 pixel square zone at the center of the image. Finally, vignetting was eliminated by adding the correction matrix to each frame obtained in the field.

https://doi.org/10.5194/amt-2020-382
Preprint. Discussion started: 26 October 2020

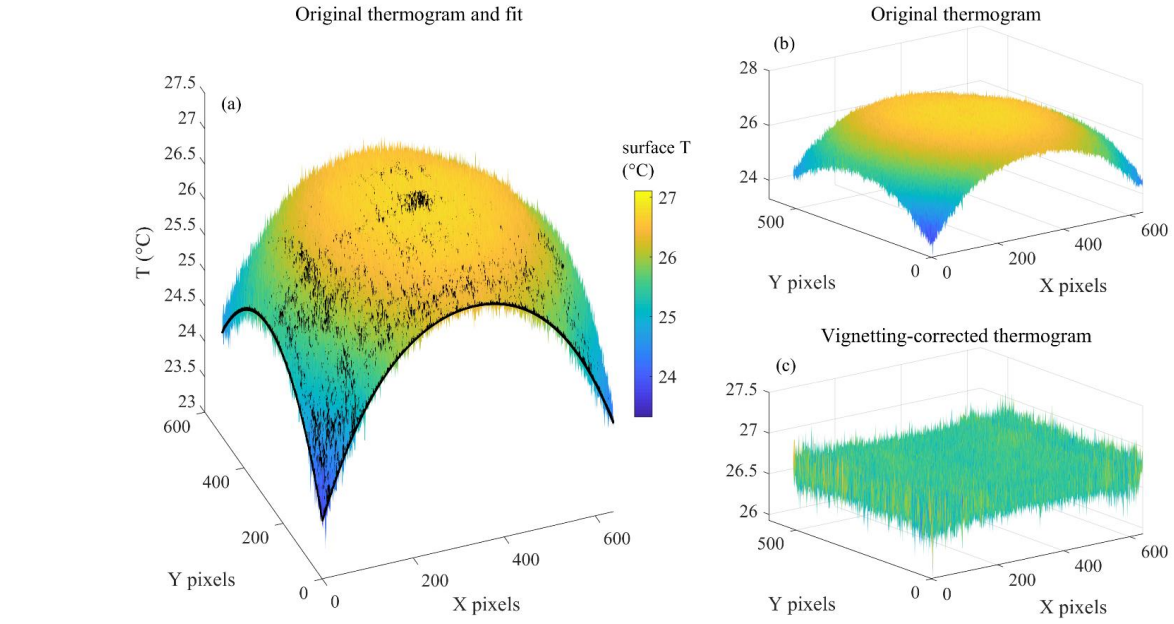

Figure A1. (a) 4th degree polynomial fit (black surface) and the thermogram of the black fabric; (b) uncorrected thermogram of black fabric surface (same data as in (a)); (c) vignetting-corrected thermogram.

Appendix B: Camera Intrinsics

The geometric calibration of the IR camera was performed using a checkerboard so as to obtain the camera intrinsic parameters given in Table B1. Figure B1 gives a screenshot of the geometric calibration process in the Matlab® Camera Calibrator tool.

Table B1. Camera intrinsic parameters.

parameter	x	y
radial distortion	-0.049	0.646
tangential distortion	0.0035	0.0028
focal length	801 mm	
principal point	327 pix	276 pix
skew	3.4796	
mean reprojection error	0.26 pix	

https://doi.org/10.5194/amt-2020-382
Preprint. Discussion started: 26 October 2020

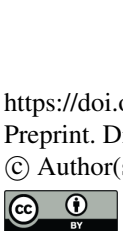

Atmospheric Measurement Techniques Discussions

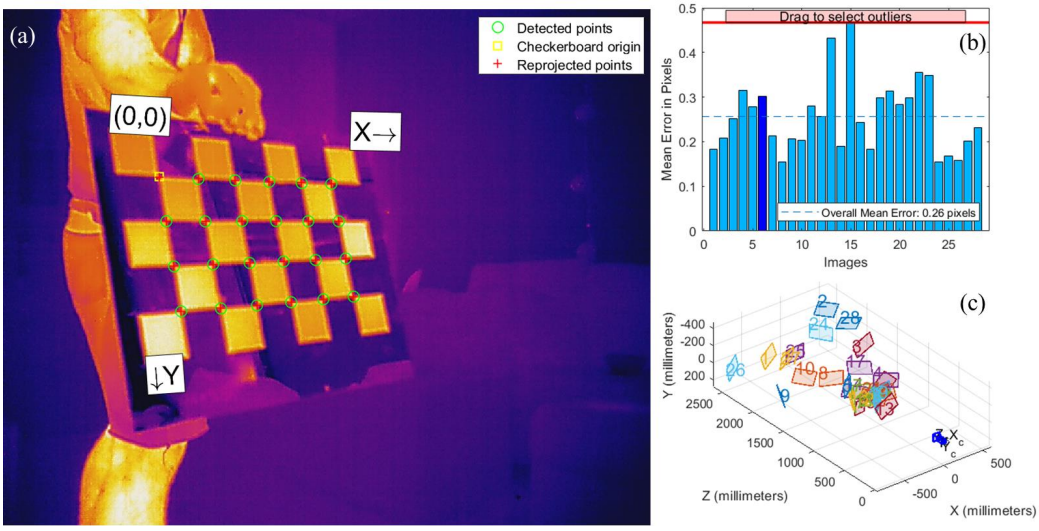

Figure B1. Screenshot from the Matlab® Camera Calibrator tool. (a) One of the 28 images used to derive the calibration parameters; (b) mean reprojection error (pix) for each image; (c) relative positions of the checkerboard relative to the camera.

Appendix C: Georeferencing

An inverse affine transform was then calculated for the reference frame of each flight to transfer it to the UTM35 co-ordinates, with the RMSE of the affine fits equaling 0.32, 0.11, 0.48, 0.43 m for the flights 1-4, respectively:

$$UTM_{lat} = -(af - ay_{pix} - cd + dx_{pix}) / (ae - bd); \quad (C1)$$

$$UTM_{lon} = (-ec + ex_{pix} + fb - by_{pix}) / (ae - bd); \quad (C2)$$

where a, b, c, d, e, f are the parameters of affine transform, x_{pix} and y_{pix} the coordinates of a pixel in an original image (with the origin in the lower left corner), and UTM_{lat} and UTM_{lon} the UTM latitude and longitude of a transformed image. As the resolution of the original images was about 0.6 m at the center, the 0.6 m resolution was preserved in the UTM grid onto which the images were transferred. As the images were co-registered in Step 3 (Sect. 2.2.3), the same set of parameters was applied to georeference each subsequent image of a sequence.

Table C1. Affine transform coefficients applied to the registered thermogram sequences of each flight along with the root-mean-squared values (RMSE).

	flight 1 **6 Aug**	**flight 2** **6 Aug**	**flight 3** **28 Aug**	**flight 4** **28 Aug**
a	-0.2536	-0.2490	-0.1683	-0.2573
b	-0.6017	-0.6057	-0.6430	-0.6124
c	352435.98	352431.41	352404.79	352425.36
d	0.6009	0.6048	0.6430	0.6124
e	-0.2533	-0.2492	-0.1659	-0.2576
f	6858603.63	6858595.52	6858569.46	6858599.99
RMSE (m)	0.32	0.11	0.48	0.43

https://doi.org/10.5194/amt-2020-382
Preprint. Discussion started: 26 October 2020

Atmospheric Measurement Techniques Discussions

Code availability

The codes are freely available at https://doi.org/10.5281/zenodo.4019155.

Data availability

The data are freely available at https://doi.org/10.5281/zenodo.4019321.

Video supplement

The visualizations of turbulence for the four flights are available at https://doi.org/10.5281/zenodo.4019175.

Video supplement link

Additionally, the videos may be watched on YouTube**,** Flight 1, 6 Aug: https://youtu.be/UwN8rFQ3Y0E, Flight 2, 6 Aug: https://youtu.be/UeNU8lq7krY, Flight 1, 28 Aug: https://youtu.be/K4ahj0EtrWM, Flight 2, 28 Aug: https://youtu.be/jgC2GDptLtU.

Author contributions

Dr. Pavel Alekseychik conceived the study, conducted the measurements and their analyses, wrote the text and produced the figures. Prof. Gabriel Katul helped develop the theoretical and analytical framework and contributed to the text. Dr. Ilkka Korpela helped develop the image processing methods and contributed to the text. Dr. Samuli Launiainen made major contributions throughout the study including theoretical and analytical methods and writing parts of the text.

Competing interests

The authors declare no competing interests.

Acknowledgements

PA and SL acknowledge the support of the projects CLIMOSS (*Climate impacts of boreal bryophytes - from functional traits to global models*) funded by the Academy of Finland, Decision no. 296116), and SOMPA *(Novel soil management practices - key for sustainable bioeconomy and climate change mitigation*, funded by the Strategic Research Council at the Academy of Finland, Decision no. 312912). Prof. Timo Vesala (INAR, University of Helsinki) is gratefully acknowledged for providing the drone and thermal camera for the use in this study.

References

Adrian, R. J.: Hairpin vortex organization in wall turbulence, Physics of Fluids 19, 041301, https://doi.org/10.1063/1.2717527, 2007.

Albertson, J. D., Parlange, M. B., Katul, G. G., Chu, C., Stricker, H. and Tyler, S.: Sensible heat flux from arid regions: A simple flux-variance method, Water Resources Research, 31, 969–973, 1995.

Alekseychik, P. K., Korrensalo, A., Mammarella, I., Vesala, T. and Tuittila, E. S.: Relationship between aerodynamic roughness length and bulk sedge leaf area index in a mixed-species boreal mire complex. Geophysical Research Letters, 44, 5836–5843. https://doi.org/10.1002/2017GL073884, 2017a.

Alekseychik, P., Mammarella, I., Karpov, D., Dengel, S., Terentieva, I., Sabrekov, A., Glagolev, M., and Lapshina, E.: Net ecosystem exchange and energy fluxes measured with the eddy covariance technique in a western Siberian bog, Atmos. Chem. Phys., 17, 9333–9345, https://doi.org/10.5194/acp-17-9333-2017, 2017b.

Christen, A., Meier, F. and Scherer, D.: High-frequency fluctuations of surface temperatures in an urban environment, Theor. Appl. Climatol., 108, 301–324, 2012.

Chudnovsky, A., Ben-Dor, E. and Saaroni, H.: Diurnal thermal behavior of selected urban objects using remote sensing measurements, Energy and Buildings, 36, 1063–1074, https://doi.org/10.1016/j.enbui ld.2004.01.052, 2004.

Fang, J. and Porté-Agel, F.: Large-eddy simulation of very-large-scale motions in the neutrally stratified atmospheric boundary layer, Boundary-Layer Meteorol., 155, 397–416, 2015.

Garai, A. and Kleissl, J.: Air and surface temperature coupling in the convective atmospheric boundary layer, J. Atmos. Sci., 68, 2945–2954, 2011.

Garai, A., and Kleissl, J.: Interaction between coherent structures and surface temperature and its effect on ground heat flux in an unstably stratified boundary layer, J. Turbul., 14, 1–23, https://doi.org/10.1080/14685248.2013.806812, 2013.

Hoyano, A., Asano, K., & Kanamaru, T.:Analysis of the sensible heat flux from the exterior surface of buildings using time sequential thermography, Atmospheric Environment, 33, 3941–3951, 1999.

Inagaki, A., Kanda, M., Onomura, S. and Kumemura, H.: Thermal Image Velocimetry, Boundary-Layer Meteorol 149**,** 1–18, https://doi.org/10.1007/s10546-013-9832-z, 2013.

Kaimal, J. C. and Businger, J. A.: Case Studies of a Convective Plume and a DustDevil, J. Appl. Meteorol.9, 612–620, 1970.

Kaimal, J. C., Wyngaard, J. C., Haugen, D. A., Cotè, O. R., Izumi, Y., Caughy, S. J., and Readings, C. J.: Turbulence structure in theconvective boundary layer, J. Atmos. Sci., 33, 2152–2169, 1976.

Kormann, R. and Meixner, F. X.: An Analytical Footprint ModelFor Non-Neutral Stratification, Bound.-Lay. Meteorol., 99, 207–224, https://doi.org/10.1023/a:1018991015119, 2001.

Laima, S., Ren, H., Li, H. and Ou, J.: Numerical Simulation of Coherent Structures in the Turbulent Boundary Layer under Diferent Stability Conditions, Energies, 13, 1068; doi:10.3390/en13051068, 2020.

Morrison, T.J., Calaf, M., Fernando, H.J.S., Price, T.A. and Pardyjak, E.R.: A methodology for computing spatiallyand temporally varying surface sensible heat flux from thermal imagery, Q.J.R. Meteorol. Soc, 143, 2616–2624, doi:10.1002/qj.3112, 2017.

Meier, F., Scherer, D., Richters, J. and Christen, A.: Atmospheric correction of thermal-infrared imagery of the 3-D urban environment acquired in oblique viewing geometry, Atmospheric Measurement Techniques, 4, 909, 2011.

Owen, P. R. and Thompson, W. R.: Heat Transfer Across Rough Surfaces, J. Fluid Mech., 15, 321–334, 1963.

Paw U, K.T., Qiu, J., Su, H.B., Watanabe, T. and Brunet, Y.: Surface renewal analysis: a new method to obtain scalar fluxes without velocity data. Agricultural and Forest Meteorology, 74, 119–137, 1995.

Priestley, C. H. B.: Turbulent Transfer in the Lower Atmosphere, University of Chicago Press, Chicago, USA, 130 pp., 1959.

Sugawara, H., Narita, K., and Mikami, T.: Estimation of effective thermal property parameter on a heterogeneous urban surface, J. Meteor. Soc. Japan, 79, 1169–1181, 2001.

Taylor, R. J.: Thermal Structures in the Lowest Layers of the Atmosphere, Aust. J. Phys. 11, 168–176, 1958.

Thielicke, W. and Stamhuis, E. J.: PIVlab – Towards User-Friendly, Affordable and Accurate Digital Particle Image Velocimetry in MATLAB, J. Open Res. Software, 2, doi:10.5334/jors.bl, 2014.

Vogt, R.: Visualisation of turbulent exchange using a thermal camera. 18th symposium on boundary layer and turbulence, Stockholm, 9-13 June 2008, Paper no. 8B.1, 2008.